NANO LETTERS
Cite This: Nano Lett. 2019, 19, 6977−6986
Letter
pubs.acs.org/NanoLett

Highly Polyvalent DNA Motors Generate 100+ pN of Force via Autochemophoresis

Aaron T. Blanchard,[†] Alisina S. Bazrafshan,[‡] Jacob Yi,[‡] Julia T. Eisman,[‡] Kevin M. Yehl,[‡,∥] Teng Bian,[§] Andrew Mugler,[§] and Khalid Salaita*[,†,‡]

[†]Wallace H. Coulter Department of Biomedical Engineering, Georgia Institute of Technology and Emory University, Atlanta, Georgia 30322, United States

[‡]Department of Chemistry, Emory University, Atlanta, Georgia 30322, United States

[§]Department of Physics, Purdue University, West Lafayette, Indiana 47907, United States

Supporting Information

ABSTRACT: Motor proteins such as myosin, kinesin, and dynein are essential to eukaryotic life and power countless processes including muscle contraction, wound closure, cargo transport, and cell division. The design of synthetic nanomachines that can reproduce the functions of these motors is a longstanding goal in the field of nanotechnology. DNA walkers, which are programmed to "walk" along defined tracks via the burnt bridge Brownian ratchet mechanism, are among the most promising synthetic mimics of these motor proteins. While these DNA-based motors can perform useful tasks such as cargo transport, they have not been shown to be capable of cooperating to generate large collective forces for tasks akin to muscle contraction. In this work, we demonstrate that highly polyvalent DNA motors (HPDMs), which can be viewed as cooperative teams of thousands of DNA walkers attached to a microsphere, can generate and sustain substantial forces in the 100+ pN regime. Specifically, we show that HPDMs can generate forces that can unzip and shear DNA duplexes (∼12 and ∼50 pN, respectively) and rupture biotin−streptavidin bonds (∼100−150 pN). To help explain these results, we present a variant of the burnt-bridge Brownian ratchet mechanism that we term autochemophoresis, wherein many individual force generating units generate a self-propagating chemomechanical gradient that produces large collective forces. In addition, we demonstrate the potential of this work to impact future engineering applications by harnessing HPDM autochemophoresis to deposit "molecular ink" via mechanical bond rupture. This work expands the capabilities of synthetic DNA motors to mimic the force-generating functions of biological motors. Our work also builds upon previous observations of autochemophoresis in bacterial transport processes, indicating that autochemophoresis may be a fundamental mechanism of pN-scale force generation in living systems.

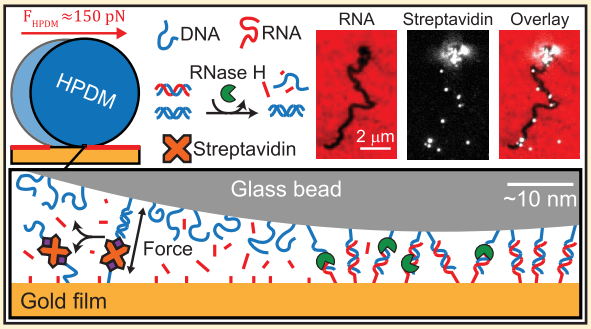

KEYWORDS: *Nanomachines, DNA nanotechnology, chemophoresis, artificial motors, DNA walkers, DNA mechanotechnology*

Walker-type DNA motors,[1−21] which use two or more DNA "feet" to translocate across nanoscale tracks, are among the most promising synthetic analogs of biological motor proteins such as myosin, kinesin, and dynein.[22] These DNA motors can be used to transport[8,12,13] and assemble[6,7] nanoscale cargo, but have not been shown to generate sustained piconewton (pN)-scale forces. Force generation is a fundamental property of biological motors, and processes such as muscle contraction, wound closure, mechanosensation, and cell motility all require collective action of many motors, each exerting 1−10 pN via ATP-fueled powerstrokes. The development of DNA-based motors that can generate pN-scale forces may enable next-generation motors and actuators that can power similar tasks.

DNA walker translocation can be described using the burnt bridge Brownian ratchet (BBBR) mechanism. This mechanism involves binding between DNA feet and complementary oligonucleotide footholds. Binding between a foot and foothold is followed by irreversible destruction of the foothold, release of the foot, and translocation of the motor to bind fresh foothold sites.[1−3] The BBBR mechanism is generally known to exhibit low chemomechanical coupling and thus produce less force per motor (∼10−100 fN as estimated via experimentally informed simulations and modeling)[23−26] than the pN-scale forces generated via the ATP-fueled powerstroke mechanism of motor proteins. Nonetheless there is, to our knowledge, no fundamental limitation on the ability of BBBR motors to cooperate and generate larger collective forces. Indeed, simulations by Samii et al. predict that increasing the polyvalency (i.e., the number of DNA feet) of a burnt-bridge

Received: June 6, 2019
Revised: August 5, 2019
Published: August 12, 2019

DOI: 10.1021/acs.nanolett.9b02311
Nano Lett. 2019, 19, 6977−6986

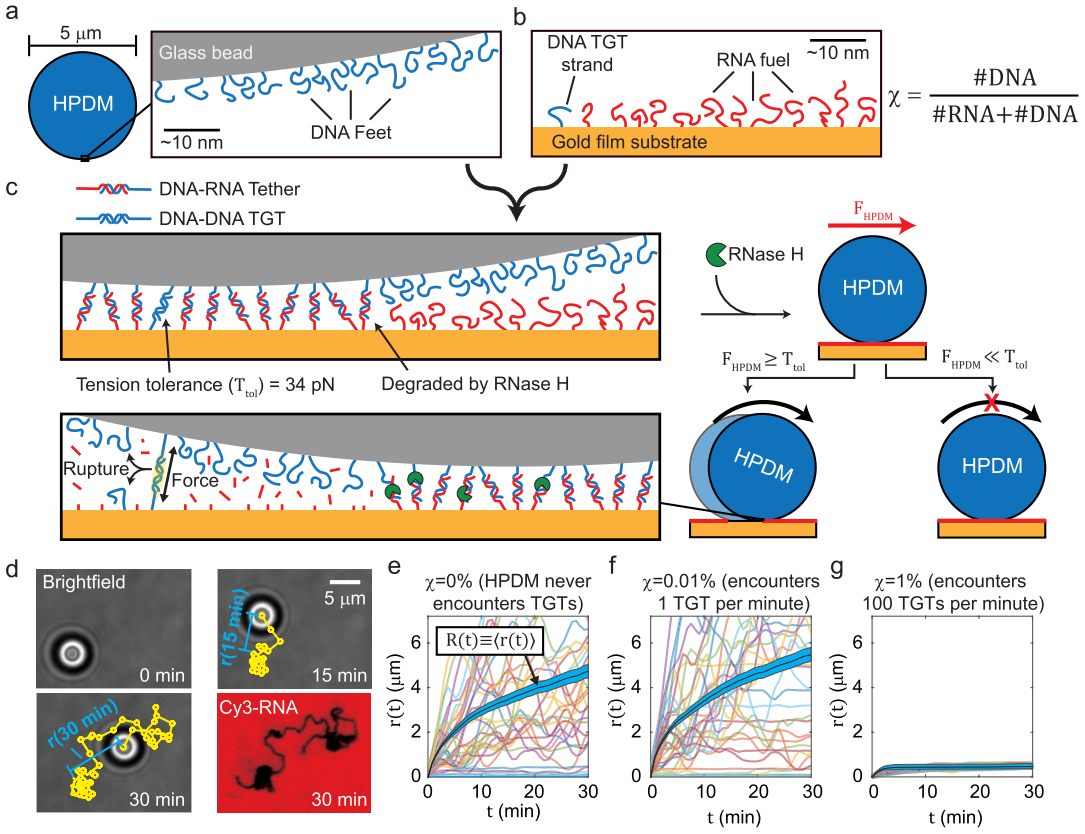

Figure 1. HPDMs mechanically rupture tension gauge tethers (TGTs). (a) HPDMs are silica (gray) microspheres coated with DNA (blue) "feet". (b) These feet bind with RNA (red) "fuel" strands that are attached to an underlying gold substrate (yellow) to form (c) "tethers" that are cleaved by the enzyme RNase H (green). We doped a small fraction (denoted by χ) of DNA strands into the RNA monolayer that also bind to DNA feet to form DNA-DNA duplexes that we refer to as TGTs. These TGTs are impervious to RNase H, so when an HPDM encounters a TGT it must generate force (denoted F_{HPDM}) surpassing the TGT's tension tolerance (T_{tol}) in order to rupture the TGT and continue moving. (d) BF microscopy snapshots of an HPDM rolling on a TGT-free substrate and a final fluorescence image of the Cy3-tagged RNA. Yellow denotes the HPDM's measured trajectory. (e–g) Displacement vs time curves, denoted $r(t)$, of 30 representative HPDMs with (e) χ = 0%, (f) χ = 0.01% (which should stall HPDM motion if $F_{HPDM} \ll T_{tol}$), and (g) χ = 1%. Black curves show the average of 700+ HPDMs per condition, denoted $R(t)$, and blue shading denotes 95% confidence interval of our estimate of $R(t)$, as calculated via 3,000 iterations of a bootstrapping algorithm. The χ = 0% condition is a negative control showing that we could demonstrate RNase H-mediated HPDM translocation in our experiment, and the χ = 1% condition is a positive control showing that TGTs can stall HPDM motion at high χ values. The χ = 0.01% condition demonstrates largely unperturbed HPDM translocation, which is consistent with the hypothesis that $F_{HPDM} \geq T_{tol}$.

motor from two to four increases the collective force generated in a linear fashion.[23] However, it is still an open question as to whether (and, if so, to what extent) cooperative force generation by multiple DNA-based motors can be implemented in practice. Herein, we demonstrate progress toward addressing this question by showing that highly polyvalent DNA motors (HPDMs), which have thousands of DNA feet, can generate and sustain 100+ pN forces. This work suggests that BBBR motors can be scaled to generate and sustain cooperative pN-scale forces.

HPDMs are DNA motors that autonomously move across planar RNA-functionalized substrates.[14] Translocating at velocities up to 5 μm/min across distances approaching the millimeter length scale, HPDMs are the fastest and most processive DNA-based motors reported thus far. An HPDM is composed of a 5 μm silica bead coated with a dense monolayer of DNA oligonucleotide feet at a surface density of ~91,000 molecules/μm^2 (Figure 1a; see Figure S1a for surface functionalization scheme). The DNA feet are complementary to RNA "fuel" strands, which are anchored to the substrate at a surface density of ~50,000 molecules/μm^2 (Figure 1b; see Figure S1b for surface functionalized scheme). When the HPDM particles are introduced to the substrate, they sediment and bind to the substrate via 15 base pair (bp) hybridization interactions between their DNA feet and the substrate's RNA fuel (which together form "tethers", Figure 1c, all sequences are listed in Table S1). The HPDMs remain stationary until the addition of ribonuclease H (RNase H), which is an enzyme that selectively hydrolyzes the phosphodiester backbone of RNA in DNA-RNA hybrid duplexes (Figure 1c). RNase H is highly specific and does not covalently modify DNA or single-stranded RNA. At standard conditions, the RNA strands in DNA-RNA tethers are cleaved at a maximal rate of k_{cat} = 25 min^{-1} (ref 14). Because there are hundreds of tethers at any given time, complete detachment from the substrate is prevented by the HPDM's high polyvalency. This combination of rapid fuel consumption and continuous substrate attachment allows HPDMs to rapidly translocate for hours or longer, consuming ~10^4 RNA fuel strands per minute (calculation in Supplemental Note 1). Due to the large size of an individual microparticle (5 μm), HPDM motion can be monitored using bright-field microscopy (BF, Figure 1d). Because RNA cleavage is irreversible, fluorescence imaging of the Cyanine-3 (Cy3)-tagged RNA fuel (Figure 1d) reveals a ~400 nm-wide

DOI: 10.1021/acs.nanolett.9b02311
Nano Lett. 2019, 19, 6977–6986

region of ~50% reduced intensity in the HPDM's wake that we call a depletion track. HPDMs generally exhibit superdiffusive motion due to depletion track avoidance, but sometimes become "self-entrapped" within their own depletion tracks and, as a result, substantially slow or stall for minutes or longer.[14] Notably, HPDMs roll as they translocate, as is most clearly illustrated by the ballistic (linear) motion of dimerized or rod-shaped HPDMs.[14]

As with conventional DNA walkers, HPDM translocation can be described using a BBBR mechanism. According to this framework, the particle initially adopts a position that maximizes the number of tethers formed. When the bound RNA is degraded by RNase H, the HPDM displays increased Brownian motion that leads to forward translocation and enables subsequent binding to new RNA fuel strands. Repetition of this cycle with thousands of tethers per minute results in forward translocation of the HPDM at μm/min-scale speeds.

Because the RNA-coated substrates lack inherent directionality (i.e., the HPDM is surrounded by fuel on all sides, save for directly behind it), we initially assumed that tethers would not act in a cooperative manner and thus assumed that HPDMs could not produce persistent forces beyond the fN range. However, we made multiple observations that were not consistent with this assumption. For example, we found that HPDMs move in a ballistic manner at subminute time scales (i.e., HPDMs travel persistently for seconds or longer, Figure S2). Because the momentum of microscale objects undergoing Brownian diffusion generally dissipates within microseconds,[27] this observation suggested that tethers act in a more cooperative manner than originally thought. Ballistic HPDM motion also resembles the persistent motion of microparticles observed by Vecchiarelli et al.[28] in studies of the bacterial partition system, wherein a BBBR mechanism generates a persistent *chemophoretic* force that can ballistically transport cargo such as plasmids across μm-scale distances. We were also unable to stall HPDM motion by doping noncleavable DNA into the RNA fuel monolayer. This second observation suggested that HPDMs were generating the 10s of pN of force required to rupture DNA duplexes.[29] Together, these results led us to hypothesize that HPDM motion is coupled to a chemophoretic driving force (F_{HPDM}) that is substantially greater than the fN-scale forces originally expected for uncoordinated DNA walkers.

To test our hypothesis that HPDMs generate pN-scale forces, we started by rigorously testing HPDMs' ability to mechanically rupture short DNA duplexes, which have well-characterized force-induced dehybridization properties, using an ensemble-level particle tracking experiment. We then compared the results of this experiment to mass-action simulation models, allowing us to estimate that HPDMs generate ~150 pN of force. To validate these findings, we next implemented single-molecule localization measurements to directly visualize DNA duplexes that have been mechanically ruptured by HPDMs. We then employed single-molecule imaging to show that HPDMs can also mechanically rupture the biotin−streptavidin bond, which is often described as the strongest noncovalent bond found in nature. We next demonstrated that HPDMs can easily rupture DNA duplexes arranged in the unzipping geometry, revealing that HPDMs can act as autonomous lithographic probes to mechanically pattern dense arrays of DNA duplexes (or "molecular ink") within the wake of their depletion tracks. Finally, we extend upon existing conceptual frameworks to help describe the mechanism of HPDM force generation, which we term autochemophoresis.

We first replaced a percentage of the RNA fuel with a DNA analog with the same sequence. We quantitatively denote this percentage as χ (Figure 1b). We anticipated that each DNA strand on the planar substrate could hybridize to a DNA foot on the surface of the HPDM, thus creating a nonhydrolyzable duplex that is akin to the tension gauge tether (TGT).[30] TGTs are stable DNA duplexes that are engineered to mechanically rupture at specific magnitudes of tension, described as the tension tolerance (T_{tol}, roughly 34 pN for a 15 bp duplex). Because TGTs irreversibly denature at specific values of T_{tol}, one application of TGTs is to quantify the minimum pN-scale forces[29,31−43] exerted by individual cell surface receptors. In our experiments, substrate-bound TGT strands display identical sequences to (and thus behave similarly to) RNA fuel strands but are immune to RNase H-mediated degradation because they form DNA-DNA duplexes. As such, feet will occasionally pair with TGT strands to form RNase H-impervious tethers, resulting in either HPDM stalling if $F_{HPDM} \ll T_{tol}$ or TGT rupture and continued HPDM motion if $F_{HPDM} \geq T_{tol}$ (Figure 1c). Note that the zero-force lifetime of a 15 bp duplex at room temperature is ~10^7 s (the zero-force activation energy barrier is ~35 k_BT, as calculated using the mathematical framework presented in ref 29). Thus, force-induced bond rupture is a requirement for continued HPDM motion after the engagement of a TGT.

We tested for force-induced rupture of TGTs at the ensemble level using a high-throughput particle tracking experiment and a custom MATLAB-based particle tracking code (Figures S3−5). As a negative control, we simultaneously tracked 721 HPDMs rolling in the absence of TGT strands (χ = 0%) for 30 min. For each HPDM, we calculated $r(t)$, which is the displacement from the initial position as a function of time (Figure 1d), and then we averaged all $r(t)$ curves to obtain $R(t)$, the ensemble average displacement as a function of time (Figures 1e and S6). We next replaced a small fraction of RNA strands with TGT strands. Based on our estimate that $k_1 = 10^4$ s^{-1} (where k_1 is the steady-state rate of tether formation, see Supplemental Note 1 for calculation), we predict that when χ = 0.01% (that is, 1 in every 10,000 RNA strands is replaced with a DNA TGT strand) HPDMs will encounter TGTs at a rate of 1 min^{-1}. In this scenario, if $F_{HPDM} \ll$ 34 pN, HPDMs will become immobilized upon encountering TGT strands and, as such, all HPDMs will be immobilized within a few minutes. In contrast, if $F_{HPDM} \geq$ 34 pN HPDMs should continue rolling processively when χ = 0.01%. We tested this by tracking 982 HPDMs on a substrate with χ = 0.01% and found that $R(t)$ was unperturbed when compared to the χ = 0% control (Figures 1f and S6), which supports the hypothesis that HPDMs can rupture TGTs. A statistical comparison of the r(30 min) populations (Figure S6) showed no difference in the median values between the χ = 0% and χ = 0.01% conditions (4.0 and 4.2 μm, respectively, p = 0.09, Wilcoxon rank sum test). As such, these results suggest that $F_{HPDM} \geq$ 34 pN. As a positive control, we found that when χ = 1% (HPDMs encounter 100 TGT strands per second) virtually no HPDM motion was observed (Figure 1g, $p < 0.001$ when compared to the r(30 min) populations with χ = 0.01% or χ = 0%, Wilcoxon rank sum test).

We next sought to quantitatively estimate F_{HPDM}. To accomplish this task, we first developed a series of mass-action

DOI: 10.1021/acs.nanolett.9b02311
Nano Lett. 2019, 19, 6977−6986

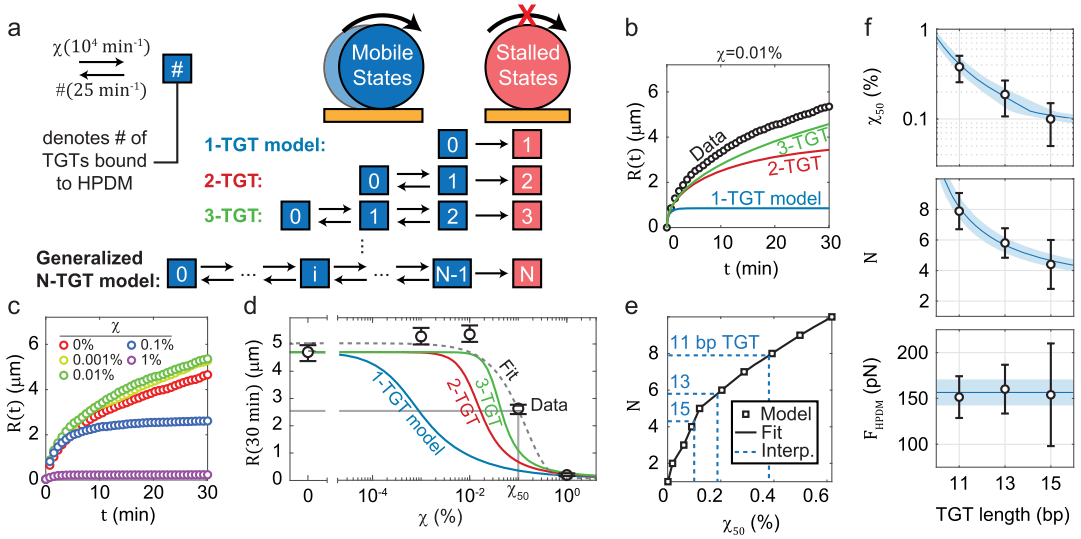

Figure 2. Quantitative estimate of F_{HPDM}. (a) Block diagrams for 1-TGT, 2-TGT, and 3-TGT simulation stall models as well as a generalized N-TGT model. In these models, all HPDMs are bound to zero TGTs at $t = 0$ and encounter TGTs at a rate of $\chi \times 10^4$ min^{-1}. HPDMs bound to fewer than N TGTs are mobile and mechanically rupture TGTs at a rate of # × 25 min^{-1}, where # denotes the number of bound TGTs, and HPDMs immediately and irreversibly stall when bound to N TGTs. (b) $R(t)$ curve measured experimentally with χ = 0.01% (circles, Figure 1d) and simulated using the 1-, 2-, and 3-TGT stall models (solid curves) shown in (a). (c) $R(t)$ curves measured experimentally with χ ranging from 0% to 1%. (d) R(30 min) with respect to χ. Exponential decay fit curve (dashed line) and best-fit χ_{50} are shown as well as simulated curves for 1-, 2-, and 3-TGT stall models (solid curves). Circles show measured data points, and error bars show the 95% confidence interval of our estimate of R(30 min), as calculated via 3,000 iterations of a bootstrapping algorithm. (e) N vs χ_{50} simulated with N-TGT models with N ranging from 1 to 10. Squares denote simulation outputs, while solid black curve shows a linear interpolation fit. Dashed blue lines show interpolations of χ_{50} values experimentally measured with 11, 13, and 15 bp TGTs. (f) Best-fit values for χ_{50} (top), N (middle), and $F_{HPDM} \approx T_{tol} \times N$ (bottom) as a function of TGT length. Error bars are 95% confidence interval of fit. Blue curves in all three subplots in (f) denote global fit value of F_{HPDM} = 157 pN, and light blue shading denotes global fit 95% confidence bounds of ±14 pN.

models to predict how $R(t)$ should change as a function of F_{HPDM} and χ (Figures 2a and S7). These models assume that the number of TGTs required to stall an HPDM should be positively correlated with F_{HPDM}. In the "1-TGT" model, a single TGT is sufficient to irreversibly stall HPDM motion (i.e., $F_{HPDM} \ll T_{tol}$). The 2-TGT model assumes that an HPDM can generate enough force to break a single TGT but cannot generate enough force to mechanically denature two TGTs simultaneously (roughly, $F_{HPDM} > T_{tol} > \frac{1}{2}F_{HPDM}$). This model produces an $R(t)$ curve that much more closely resembles the experimentally observed result (Figure 2b). Further still, the 3-TGT model, in which HPDMs are mobile when bound to 0, 1, or 2 TGTs but stall when bound to 3-TGTs, nearly predicts the observed unperturbed behavior because simultaneous encounter of 3 TGTs is rare when χ = 0.01% (Figure 2b). These results suggest that HPDMs consistently rupture TGTs and may even be strong enough to rupture three or more TGTs simultaneously, indicating that $F_{HPDM} \geq 102$ pN.

Note that, although we performed statistical comparison of population medians (which are more appropriate to report than population means for skewed distributions such as ours), we chose to display and analyze population means because the N-TGT models can only predict expected changes in mean displacement vs time curves. A similar modeling approach that predicts the expected population median as a function of time would not be accurate because, in short, the median is not a linear operator and our models rely on the use of linear mathematical operations.

We next performed particle tracking of HPDMs on substrates with χ ranging from 0.001% to 1% (Figures 2c and S8). While no significant differences in the median r(30 min) values were observed between the χ = 0.001% population (median of 4.1 μm) and the χ = 0% or χ = 0.01% populations (p = 0.19 and p = 0.65, respectively, Wilcoxon rank sum test), the χ = 0.1% and χ = 1% populations had median r(30 min) values (1.6 and 0.03 μm, respectively) that were significantly different from all other tested conditions ($p < 0.001$, Wilcoxon rank sum test). We then performed parameter fitting on the combined data sets to estimate χ_{50}, which is the χ that leads to a 50% reduction of R(30 min) (Figures 2d, S6, and S8). The best-fit χ_{50} of 0.10% ± 0.05% (bounds denote 95% confidence interval) is ∼100-fold greater than the 1-TGT model's prediction of χ_{50} = 0.0011%, whereas the 2-TGT model more accurately predicts χ_{50} = 0.018% and the 3-TGT model predicts an even more accurate χ_{50} 0.061%. We then used the output of our N-TGT simulations and linear interpolation (Figure 2e, S9) to back-calculate N as a function of χ_{50} and estimated that N = 4.4 ± 1.6 TGTs are required to stall a single HPDM, allowing us to obtain a crude approximation of $F_{HPDM} \approx N \times T_{tol}$ = 154 ± 56 pN (Figure 2f). In Supplemental Note 2, we show that this approximation is reasonable because T_{tol} should accurately reflect the average force at which HPDMs rupture duplexes. For our N-TGT simulations, we assume that TGTs form at a rate of $\chi \times k_1 = \chi \times 10^4$ min^{-1} and rupture at a rate of k_2 = 25 min^{-1}. In Supplemental Note 3 we show that, although HPDMs likely take 20+ seconds to extend and rupture TGTs (which is much longer than k_2^{-1} = 2.4 s), the use of k_2 is still reasonable because TGTs must form within a few seconds of each other in order for their resistive forces to contribute collectively to HPDM stalling.

Repeating these experiments and calculations with weaker 13 or 11 bp TGTs (T_{tol} = 28 pN and 19 pN, respectively)

DOI: 10.1021/acs.nanolett.9b02311
Nano Lett. 2019, 19, 6977−6986

increased χ_{50} (0.19% ± 0.08% and 0.38% ± 0.12%) and thus increased N (5.8 ± 1.0 and 7.9 ± 1.2) in a manner that kept F_{HPDM} fairly constant at 160 ± 26 pN and 152 ± 23 pN, respectively (Figures 2f and S10). A global fit of these combined data sets yielded F_{HPDM} = 157 ± 14 pN. Our estimate of $F_{HPDM} \approx 157$ pN indicates that HPDMs possess a peak chemical energy to mechanical energy conversion efficiency of ~3.6% (Supplemental Note 4), which is roughly an order of magnitude lower than that of cytoskeletal motors but several orders of magnitude higher than our previous estimate (and could potentially be increased through optimization). Impressively, this estimate suggests that HPDMs have a force-generating capacity that far surpasses that of individual cytoskeletal walkers (1−10 pN) and even the bacterial pilus machine,[44] which is the strongest-reported molecular motor (100 pN).

To obtain more direct evidence for force-induced duplex rupture by HPDMs, we pre-assembled biotin-terminated 25 bp TGTs (T_{tol} = 49 pN) on HPDMs and linked an Alexa 647 fluorophore (A647)-functionalized streptavidin molecule to the terminus of each TGT through biotin−streptavidin binding (Figure 3a,b). We also replaced ~10% of RNA fuel strands on the underlying surface with biotin-presenting DNA strands. Streptavidin is a globular protein that can form high affinity bonds with up to four biotin molecules simultaneously. As such, HPDM motion will occasionally lead to biotin−streptavidin cross-linking between a TGT's terminal streptavidin and a biotin attached to the underlying surface. The resulting linkage contains a rupturable TGT duplex and two biotin−streptavidin bonds. The T_{tol} of a biotin−streptavidin bond is ~147 pN (see Methods in the Supporting Information for calculation), making it substantially stronger than even the strongest DNA duplexes and one of the strongest noncovalent bonds found in nature. Therefore, as in the experiments described above, formation of one of these linkages will either be followed by HPDM stalling, if $F_{HPDM} \ll 49$ pN, or TGT rupture and continued HPDM motion, if $F_{HPDM} \geq 49$ pN. However, in this case TGT rupture will also result in deposition of the fluorescent streptavidin molecule onto the substrate. Therefore, if $F_{HPDM} \geq 49$ pN, then HPDM depletion tracks will be dotted with fluorescent streptavidin molecules that can be directly visualized via single-molecule localization microscopy. As in previous studies that utilize TGTs, fluorescent streptavidin images can thus be loosely interpreted as reporting the cumulative history of HPDM force. The frequency of biotin−streptavidin engagement will depend on the percent of DNA feet that have been replaced with streptavidin-capped TGTs, which we denote as χ'. The quantity χ' is functionally very similar to χ as defined above (see Methods and Figure S11 for a description of how we calculated χ').

As expected, we observed highly processive HPDM motion along with the periodic deposition of streptavidin within depletion tracks using single-molecule localization microscopy when χ' = 0.5% (Figures 3c, S12, and S13). While some localizations did appear outside of depletion tracks, quantitative analysis of ~100 HPDMs' depletion tracks revealed a 40-fold enhancement of localization density within depletion tracks when compared to the background ($p < 0.001$, paired t test, Figures 3e and S14). When repeating this experiment in the absence of either HPDM-bound TGT strands or substrate-bound biotin-presenting strands, we observed no significant change in localization density within depletion tracks ($p >$

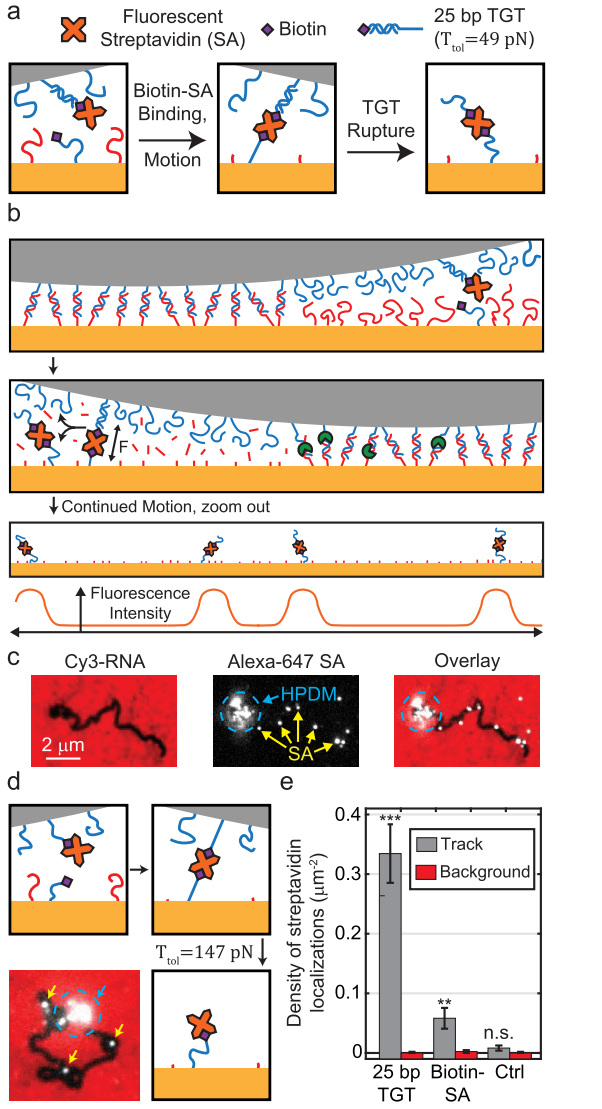

Figure 3. Single-molecule imaging of bond rupture driven by HPDM force generation. (a, b) Cartoons depicting force sensor function. Fluorescent streptavidin-capped TGTs are pre-assembled on HPDMs, and as the HPDMs translocate, the streptavidin molecules bind to surface-tethered biotin strands. Subsequent movement by the HPDM then generates enough force to rupture the TGT, and the deposited streptavidin molecules can be visualized using single-molecule fluorescence microscopy. (a) Zoom-in on single force sensor and (b) expanded view. (c) Cy3-RNA fluorescence image (left) and A647-streptavidin image with streptavidin molecules denoted using yellow arrows. The HPDM, which has several SA localizations associated with it and therefore produces substantial background signal, is shown using a blue arrow and a dashed blue circle. An overlay (right) shows co-localization between the depletion track and streptavidin molecules. (d) Cartoon depiction and representative data for experimental test of biotin−streptavidin bond rupture. (e) Surface density of single streptavidin molecule localizations in depletion tracks (gray) and the background (red) for 25 bp TGT (χ' = 0.5%) and biotin−streptavidin (χ' = 0.03%) rupture experiments as well as a control experiment conducted with biotin-lacking HPDMs. Results of statistical comparison (paired t test) between depletion track and background localization densities are shown, where ** denotes $p < 0.01$, *** denotes $p < 0.001$, and n.s. denotes $p > 0.05$. Error bars are standard error of the mean. Fluorescence images in (c) and (d) were filtered with rolling-ball background normalization and contrast enhancement to better highlight depletion tracks and single molecules.

DOI: 10.1021/acs.nanolett.9b02311
Nano Lett. 2019, 19, 6977−6986

0.05, paired t test), indicating minimal (if any) contribution of the shedding of nonspecifically bound streptavidin molecules to the observed result (Figures 3e and S14).

We next tested whether HPDMs are capable of rupturing biotin–streptavidin bonds by replacing the biotin-terminated TGT in the above experiment with a biotin-terminated DNA strand that is covalently linked to the HPDM (Figure 3d). Following biotin–streptavidin binding, the HPDM can only continue rolling if it mechanically ruptures one of the two biotin–streptavidin bonds (T_{tol} = 147 pN), resulting in deposition of a streptavidin molecule with 50% probability. As with the TGTs, we observed a 10-fold increase in streptavidin localization density within these depletion tracks when χ' = 0.03% ($p < 0.01$, paired t test, Figures 3d,e and S15). These localizations tended to be surrounded by "depletion patches" that were significantly wider than the 400 nm width of typical depletion tracks, indicating that HPDMs may execute extended searches to generate the force necessary to rupture biotin–streptavidin bonds. Via high-throughput tracking, we found that χ'_{50} = 0.08 ± 0.06%. When dividing this quantity by 10 (reflecting that only 10% of substrate RNA was replaced with biotin-presenting strands) and interpolating into our N-TGT simulation models, we found that N = 1.4 ± 0.3 molecules and F_{HPDM} = 207 ± 48 pN (Figure S16). We expect that this estimate of F_{HPDM} is an overestimation because the N-TGT models were constructed assuming that HPDM velocity is unperturbed by bond engagement, which is likely not true in this case because T_{tol} is similar to F_{HPDM}. This hypothesis is supported by the observation of depletion patches and the finding that $1 < N < 2$. As stated above, when repeating these single-molecule experiments in the absence of surface-bound biotin, we generally observed no significant enhancement of localizations within depletion tracks (Figures 3e and S13) or HPDM stalling, thus confirming that streptavidin localizations represent HPDM-mediated and force-induced deposition.

A TGT's T_{tol} depends not only on length and sequence but also on the pulling geometry. All TGTs discussed thus far have been arranged in the "shear" mode, wherein force is applied to opposite ends of the DNA duplex (e.g., 5′-5′ or 3′-3′). This pulling geometry maximizes T_{tol} because duplex rupture requires simultaneous denaturation of all base pairs. However, when force is applied to the same end of the duplex (e.g. 3′-5′), base pairs are unzipped one-at-a-time and, as such, T_{tol} is minimized. In other words, while T_{tol} = 49 pN for a 25 bp TGT in shear-mode, T_{tol} = 12 pN for the same 25 bp TGT in unzip mode[30] (Figure 4a). Our previous results suggest that flipping the orinetation of the TGT from shear-mode to unzip-mode (Figure 4b) should enable HPDMs to continue translocating even when bound to several (e.g. 10 or more) TGTs. As such, we predicted that we would observe processive HPDM motion at much higher χ' values, which would enable the deposition of much more dense layers of streptavidin molecules (rather than periodic, isolated molecules) within HPDM depletion tracks.

As expected, HPDMs with unzip-mode TGTs displayed highly processive motion with χ' = 5.3% (Figures 4c and S16). In contrast, HPDMs coated with shear-mode TGTs with χ' = 4.4% displayed no motion (Figure S16). Furthermore, fluorescence microscopy revealed that unzip-mode TGT-coated HPDMs left dense trails of fluorescent streptavidin in their depletion tracks (Figures 4c and S17). Quantitative analysis revealed that ~23% of all depletion track area was associated with high streptavidin fluorescence signal, compared

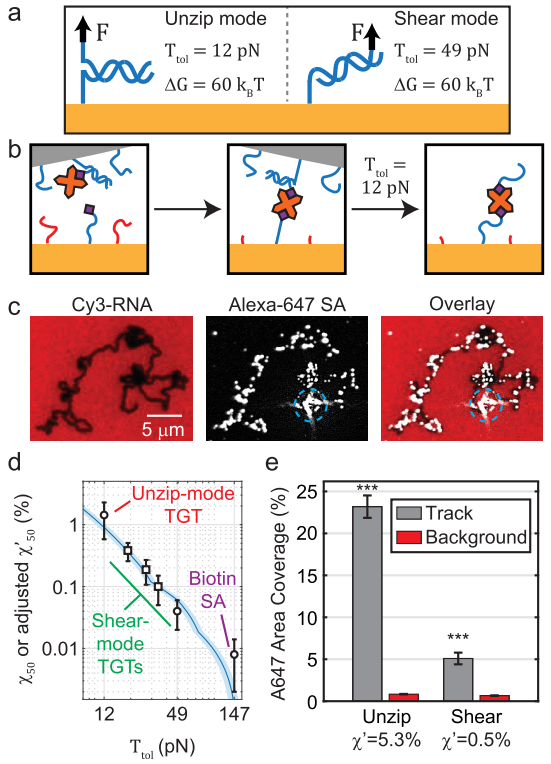

Figure 4. HPDM-mediated nanopatterning enabled by unzip-mode TGT rupture. (a) Cartoon illustration of the difference between shear-mode and unzip-mode TGTs. While the two types of TGTs have the same free energy of hybridization (ΔG), they have different T_{tol} due to differences in the kinetic pathways of dehybridization. (b) Cartoon depicting unzip-mode TGTs in the context of our experiment. (c) Representative fluorescence microscopy images showing that HPDMs leave a dense trail of SA in their depletion tracks. The SA image was processed with rolling ball background subtraction, and both images were contrast-enhanced for clarity. (d) Log–log plot of best-fit χ_{50} (squares) or χ'_{50} adjusted by dividing by 10 (circles) as a function of T_{tol}. Circle and squares denote best-fit values obtained from fits to experimental data, bounds denote 95% confidence interval of the fit, and the blue curve and shading represent the global fit to the N-TGT simulation output corresponding to F_{HPDM} = 157 ± 14 pN.

with 0.7% of the background area (~30-fold enhancement; this is likely also an underestimate, see Figure S18). We used area coverage for this analysis, rather than the surface density of single-molecule localizations, because the high density of streptavidin molecules generally made it impossible to discriminate individual molecules. Applying the same analysis to shear-mode depletion tracks at the highest χ' where substantial HPDM motion was observed (χ' = 0.5%) revealed a more modest ~6% coverage (~10-fold enhancement over background, Figure S18). While these two data sets were collected on different days with different χ' values, we also performed a side-by-side comparison of data collected on the same day with similar χ' values and found that the depletion tracks of HPDMs with unzip-mode TGTs were significantly brighter in the A647 channel those of HPDMs with shear-mode TGTs ($p < 0.001$, Figure S19).

We also performed high-throughput tracking and parameter fitting of HPDMs coated with shear- and unzip-mode 25 bp TGTs and found that χ'_{50} = 0.4% ± 0.2% and 14.3% ± 8.5%, respectively. We divided these quantities by 10 and performed global fitting to the combined data sets as described above

DOI: 10.1021/acs.nanolett.9b02311
Nano Lett. 2019, 19, 6977–6986

(Figures 2e and S16) and found that $N = 3.3 \pm 1.1$ for shear-mode TGTs and $N = 13.4 \pm 4.6$ for unzip-mode TGTs, with $F_{HPDM} = 160 \pm 55$ pN. These quantitative estimates are consistent with those obtained throughout this work, and the 230-fold difference in χ'_{50} between the two TGT modes is consistent with the notion that F_{HPDM} is consistent between experiments and is sufficient to drive TGT and biotin–streptavidin rupture. Adding these data sets to the 11 bp, 13 bp, and 15 bp TGT data sets described above yielded an (unchanged) global fit of $F_{HPDM} = 157 \pm 14$ pN.

These results demonstrate conclusively that SA deposition is indeed a result of force-induced bond rupture. Furthermore, these results demonstrate the potential of HPDMs to serve as autonomous nanopatterning machines; nanopatterning is commonly performed using externally controlled motors (e.g., by using an atomic force microscope to perform dip-pen nanolithography[45] or cut-and-paste surface assembly[46]), but HPDMs can autonomously create nanoscale patterns of "molecular ink" via force-induced bond rupture without an externally controlled motor.

An HPDM is a rigid scaffold connecting many independent DNA feet that autonomously coordinate to generate substantial forces while translocating on nondirectional substrates. To better understand how HPDMs generate such large forces, we revisit the BBBR framework discussed above. However, for this discussion, rather than focusing on the biased Brownian motion of the microparticle, we slightly reframe our discussion to focus on individual tethers and the effect that they have on the microparticle. We define "backwards" and "forwards" HPDM movement as motion toward and away from the depletion track, respectively, and define "leftward" and "rightward" motion as opposing 90° turns from the forward and backward directions.

Considering each tether to act as an entropic spring (e.g., using the worm-like-chain model)[47−49] with a thermodynamic drive to minimize its end-to-end extension reveals a mechanical driving force that we had not previously considered; when a new tether forms, the tether immediately begins exerting an entropic tensile force on the HPDM. Force balance principles dictate that this new force creates a force imbalance that is only resolved upon movement and reorientation of the HPDM (Figure 5). In other words, when a tether forms, it immediately shifts the HPDM's energetic minimum position and orientation. Because this is the step at which chemical energy (released from the hybridization interaction) is converted into mechanical work that moves the HPDM, we contend that tether formation represents the force-generating powerstroke of HPDM motion. Note that we use the term powerstroke in its broadest definition (meaning "the stroke of a cyclic motor which generates force"). This broad definition applies to motors across all length scales (e.g., macroscopic to molecular-scale), so the use of the term powerstroke here should not be interpreted as strictly relating to a powerstroke model of cytoskeletal motor proteins.

Force-balance principles also dictate that HPDM movement following tether formation necessarily results in the extension of some "resistive" tethers, such that the work performed by the new tether is converted into mechanical strain energy and stored in these resistive tethers. The eventual cleavage of these resistive tethers releases the mechanical strain energy stored within them in a manner that resembles the release of energy after a stretched rubber band is cut, thus resulting in additional motion of the HPDM (Figure 5). Because there is a surface

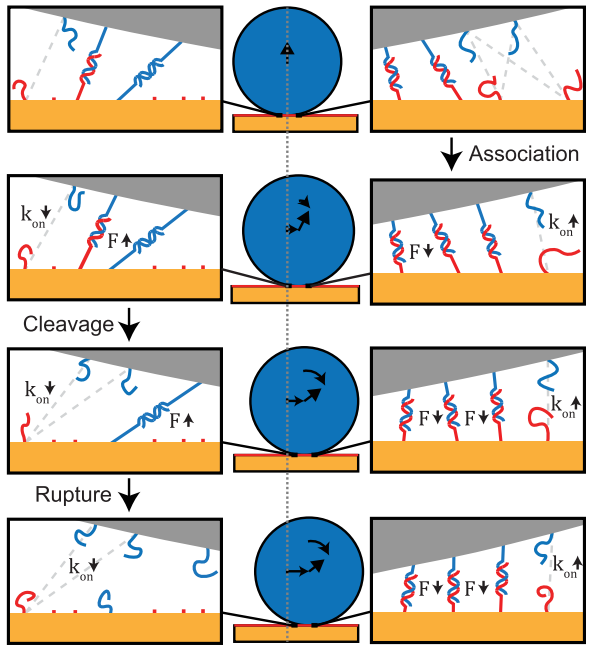

Figure 5. HPDMs generate force through autochemophoresis. When a new tether forms, it begins exerting an adhesive force on the HPDM, resulting in movement and reorientation that results in the extension of resistive tethers. Tether formation is biased away from the depletion region due to the RNA surface density gradient, which is self-propagated by the HPDM. Forward HPDM movement increases the on rate (k_{on}) of strands in the direction of movement (shown on the right) while decreasing k_{on} for strands at the back end of the HPDM (shown on the left), creating a positive feedback loop that promotes further forward motion. Cleavage of resistive tethers also releases stored mechanical strain energy that allows further forward motion of the particle. The repetition of many of these events can cause the force (F) on a TGT to eventually increase to the point of bond rupture.

density gradient of RNA fuel in the HPDM's vicinity (e.g., there is more RNA fuel in front of the HPDM than behind it), tether formation is more likely to occur at the forward-facing edge of the particle and result in forward motion. In contrast, because there is generally no surface density gradient of RNA fuel from left to right (or vice versa), sideways motion is less favorable than forward motion. Because forward motion is generally favored, resistive tethers will generally be stretched in a manner that causes them to resist forward motion. As such, it follows that the cleavage of tethers also generally favors forward motion. Forward motion also decreases the distance between unpaired DNA feet and RNA fuel at the front-edge of the HPDM, thus increasing the rate of tether formation at the front edge (Figure 5). The reverse is also true; forward motion increases the distance between feet and fuel strands at the backward-facing edge of the HPDM and thus decreases their association rate. This framework also leads to the prediction that these interacting chemical and mechanical processes result in a positive feedback loop that allow the tethers to spontaneously cooperate to generate relatively large collective forces (Figure 5). These processes also likely contribute to the persistence observed by HPDMs (Figure S2) and have been discussed previously in relation to the bacterial partition system in other works. In particular, we refer readers to work by Hu et al.,[50] in which detailed simulations are used to illustrate many of the points discussed here in greater detail.

DOI: 10.1021/acs.nanolett.9b02311
Nano Lett. 2019, 19, 6977−6986

We have principally discussed our conceptual understanding of how tethers control the energetic minimum position and orientation of an HPDM. While we have largely ignored the effect of thermal (Brownian) fluctuations of the microparticle body, we argue that it is reasonable to do so because the Brownian motion of the microparticle body is highly restricted at high polyvalency; calculations suggest that when the particle is only bound to 1 tether, it can diffuse freely within a ∼22 nm-wide volume (Figure S20). However, when an HPDM is bound to ∼100 tethers, diffusion is restricted to a ∼3.5 nm-wide volume (Figure S20). Regardless of polyvalency, the RNA and DNA oligonucleotides themselves undergo thermal fluctuations that allow them to stretch out and pair with strands within a binding cutoff distance (the separation distance below which a foot strand and fuel strand can hybridize) of ∼10 nm (Figure S20). Put another way, at low polyvalency, motion is driven by ratcheted Brownian fluctuations of the particle body as well as the oligonucleotides, but at high polyvalency, Brownian fluctuations of the particle body are quenched and motion is primarily driven by ratcheted Brownian fluctuations of the oligonucleotides. In Supplemental Note 5, we perform calculations that suggest that the transition between these two types of motion occurs gradually with increasing polyvalency, with a crossover point at which the two types of Brownian fluctuations contribute equally occurring at a polyvalency of ∼50 tethers.

Adhesion-driven movement of cargo up a concentration gradient has previously been studied and is called chemophoresis.[51] Because an HPDM moves via a self-propagated chemophoretic energy gradient,[52] we introduce the more precise term *autochemophoresis* to describe the mechanism of HPDM motion. The bacterial partition system, which plays vital roles in plasmid and chromosome replication and protein cluster positioning, can also be classified as autochemophoretic.[28,50,51,53−61] This mechanism has been called a third fundamental form of directed subcellular cargo transport (along with cytoskeletal stepping and filament polymerization) and is speculated to play roles in various biological processes such as virus−host association.[28] However, autochemophoresis has not been explicitly studied in terms of pN-scale force generation and is generally assumed to be restricted to the fN range, which is sufficient to transport nanoscale cargo through the cellular environment but not to perform many useful tasks such as cellular contraction, chromosome separation, and mechanosensation. Given the simplicity of the components required for autochemophoresis and the findings presented herein, we speculate that autochemophoresis may also be a significant mechanism of pN-scale force generation in biological systems. This means that autochemophoresis may play roles in biological processes that extend beyond cargo transport, including mechanotransduction, contraction, and protrusion. Because HPDMs are fully synthetic and have many properties that can be easily tuned, we anticipate that they will be useful in future studies aimed at understanding the fundamental principles of autochemophoresis.

To the best of our knowledge, this is the first demonstration of a DNA-based motor generating pN-scale force to perform useful tasks such as bond rupture and nanopatterning. Force generation is a fundamental aspect of biological motors that has been elusive to the field of DNA nanotechnology. Note that HPDMs generate forces through the collective action of thousands of oligonucleotides. Therefore, our findings demonstrate that future generations of DNA walkers,[1−21] other hybridization-based DNA machines,[21,62−67] and non-DNA-based burnt bridge molecular motors[68] can be used for engineering application that require pN-scale force generation. The diversity and potential of such engineering applications are illustrated by the ubiquity of biological motors like myosin and kinesin in eukaryotes[22] and nanotechnology.[69,70] HPDMs are part of a growing trend towards the development of DNA-based devices that sense, transmit, and generate forces. The rate of growth of this emerging field, which we call DNA mechanotechnology,[71] suggests that force generating DNA-based nanomachines will play increasingly important roles in diverse areas including biological research and materials science. While existing HPDMs are relatively large, with diameters of ∼5 microns, the contact junction is only 400 nm wide. As such, we anticipate that the properties of autochemophoretic force generation should scale down to the nanoscale. In future works, we will test this hypothesis with the aim of developing nanoscale HPDMs that can perform previously impossible tasks such as the powering of nanomotors and deformation of nanoscale objects.

■ ASSOCIATED CONTENT

Supporting Information

The Supporting Information is available free of charge on the ACS Publications website at DOI: 10.1021/acs.nanolett.9b02311.

Experimental and computational methods and supplemental figures, notes, and table (PDF)

■ AUTHOR INFORMATION

Corresponding Author

*E-mail: k.salaita@emory.edu.

ORCID

Khalid Salaita: 0000-0003-4138-3477

Present Address

‖Department of Biological Engineering, Massachusetts Institute of Technology, Cambridge, Massachusetts 02139, United States

Notes

The authors declare no competing financial interest.

■ ACKNOWLEDGMENTS

This work is supported by the National Science Foundation (NSF) 1611102 (K.S.), National Institute of General Medical Sciences (NIGMS) R01 GM124472 (K.S.), NSF CAREER 1350829 (K.S.), and NSF GRFP DGE-1444932 (A.T.B). We thank Emory Physics professors Eric Weeks and Laura Finzi for helpful conversations, and we thank Emory Physics professor Justin Burton for providing us with access to his laser cutter. We also thank Emory Physics professor Sergei Urazhdin and his research assistants Andrei Zholud and Ryan Freeman for access to and operational assistance with their thermal evaporator.

■ REFERENCES

(1) Sherman, W. B.; Seeman, N. C. *Nano Lett.* **2004**, *4* (7), 1203−1207.

(2) Yin, P.; Yan, H.; Daniell, X. G.; Turberfield, A. J.; Reif, J. H. *Angew. Chem., Int. Ed.* **2004**, *43* (37), 4906−4911.

(3) Shin, J.-S.; Pierce, N. A. *J. Am. Chem. Soc.* **2004**, *126* (35), 10834−10835.

DOI: 10.1021/acs.nanolett.9b02311
Nano Lett. 2019, 19, 6977−6986

(4) Bath, J.; Green, S. J.; Turberfield, A. J. *Angew. Chem., Int. Ed.* **2005**, *44* (28), 4358−4361.
(5) Omabegho, T.; Sha, R.; Seeman, N. C. *Science* **2009**, *324* (5923), 67.
(6) He, Y.; Liu, D. R. *Nat. Nanotechnol.* **2010**, *5*, 778.
(7) Gu, H.; Chao, J.; Xiao, S.-J.; Seeman, N. C. *Nature* **2010**, *465*, 202.
(8) Lund, K.; Manzo, A. J.; Dabby, N.; Michelotti, N.; Johnson-Buck, A.; Nangreave, J.; Taylor, S.; Pei, R.; Stojanovic, M. N.; Walter, N. G.; Winfree, E.; Yan, H. *Nature* **2010**, *465*, 206.
(9) Wang, Z.-G.; Elbaz, J.; Willner, I. *Nano Lett.* **2011**, *11* (1), 304−309.
(10) Wickham, S. F. J.; Bath, J.; Katsuda, Y.; Endo, M.; Hidaka, K.; Sugiyama, H.; Turberfield, A. J. *Nat. Nanotechnol.* **2012**, *7*, 169.
(11) You, M.; Chen, Y.; Zhang, X.; Liu, H.; Wang, R.; Wang, K.; Williams, K. R.; Tan, W. *Angew. Chem., Int. Ed.* **2012**, *51* (10), 2457−2460.
(12) Cha, T.-G.; Pan, J.; Chen, H.; Salgado, J.; Li, X.; Mao, C.; Choi, J. H. *Nat. Nanotechnol.* **2014**, *9*, 39.
(13) Zhou, C.; Duan, X.; Liu, N. *Nat. Commun.* **2015**, *6*, 8102.
(14) Yehl, K.; Mugler, A.; Vivek, S.; Liu, Y.; Zhang, Y.; Fan, M.; Weeks, E. R.; Salaita, K. *Nat. Nanotechnol.* **2016**, *11*, 184.
(15) Jung, C.; Allen, P. B.; Ellington, A. D. *Nat. Nanotechnol.* **2016**, *11*, 157.
(16) Wang, L.; Deng, R.; Li, J. *Chem. Sci.* **2015**, *6* (12), 6777−6782.
(17) Dannenberg, F.; Kwiatkowska, M.; Thachuk, C.; Turberfield, A. J. *Nat. Comput.* **2015**, *14* (2), 195−211.
(18) Yang, X.; Tang, Y.; Mason, S. D.; Chen, J.; Li, F. *ACS Nano* **2016**, *10* (2), 2324−2330.
(19) Thubagere, A. J.; Li, W.; Johnson, R. F.; Chen, Z.; Doroudi, S.; Lee, Y. L.; Izatt, G.; Wittman, S.; Srinivas, N.; Woods, D.; Winfree, E.; Qian, L. *Science* **2017**, *357* (6356), eaan6558.
(20) Qu, X.; Zhu, D.; Yao, G.; Su, S.; Chao, J.; Liu, H.; Zuo, X.; Wang, L.; Shi, J.; Wang, L.; Huang, W.; Pei, H.; Fan, C. *Angew. Chem., Int. Ed.* **2017**, *56* (7), 1855−1858.
(21) Urban, M. J.; Both, S.; Zhou, C.; Kuzyk, A.; Lindfors, K.; Weiss, T.; Liu, N. *Nat. Commun.* **2018**, *9* (1), 1454.
(22) Schliwa, M.; Woehlke, G. *Nature* **2003**, *422*, 759.
(23) Samii, L.; Blab, G. A.; Bromley, E. H. C.; Linke, H.; Curmi, P. M. G.; Zuckermann, M. J.; Forde, N. R. *Phys. Rev. E* **2011**, *84* (3), No. 031111.
(24) Olah, M. J.; Stefanovic, D. *Phys. Rev. E* **2013**, *87* (6), No. 062713.
(25) Samii, L.; Linke, H.; Zuckermann, M. J.; Forde, N. R. *Phys. Rev. E* **2010**, *81* (2), No. 021106.
(26) Morozov, A. Y.; Pronina, E.; Kolomeisky, A. B.; Artyomov, M. N. *Phys. Rev. E* **2007**, *75* (3), No. 031910.
(27) Poon, W. C. K., Andelman, D. *Soft Condensed Matter Physics in Molecular and Cell Biology*; CRC Press: Boca Raton, FL, 2006; p 163.
(28) Vecchiarelli, A. G.; Neuman, K. C.; Mizuuchi, K. *Proc. Natl. Acad. Sci. U. S. A.* **2014**, *111* (13), 4880.
(29) Mosayebi, M.; Louis, A. A.; Doye, J. P. K.; Ouldridge, T. E. *ACS Nano* **2015**, *9* (12), 11993−12003.
(30) Wang, X.; Ha, T. *Science* **2013**, *340* (6135), 991.
(31) Albrecht, C.; Blank, K.; Lalic-Multhaler, M.; Hirler, S.; Mai, T.; Gilbert, I.; Schiffmann, S.; Bayer, T.; Clausen-Schaumann, H.; Gaub, H. E. *Science* **2003**, *301* (5631), 367−70.
(32) Wan, Z.; Chen, X.; Chen, H.; Ji, Q.; Chen, Y.; Wang, J.; Cao, Y.; Wang, F.; Lou, J.; Tang, Z.; Liu, W. *eLife* **2015**, *4*, No. e06925.
(33) Chowdhury, F.; Li, I. T. S.; Leslie, B. J.; Doğanay, S.; Singh, R.; Wang, X.; Seong, J.; Lee, S.-H.; Park, S.; Wang, N.; Ha, T. *Integr. Biol.* **2015**, *7* (10), 1265−1271.
(34) Wang, X.; Sun, J.; Xu, Q.; Chowdhury, F.; Roein-Peikar, M.; Wang, Y.; Ha, T. *Biophys. J.* **2015**, *109* (11), 2259−2267.
(35) Wang, X.; Rahil, Z.; Li, I. T. S.; Chowdhury, F.; Leckband, D. E.; Chemla, Y. R.; Ha, T. *Sci. Rep.* **2016**, *6*, 21584.
(36) Roein-Peikar, M.; Xu, Q.; Wang, X.; Ha, T. *Phys. Rev. X* **2016**, *6* (1), No. 011001.
(37) Liu, Y.; Blanchfield, L.; Ma, V. P.-Y.; Andargachew, R.; Galior, K.; Liu, Z.; Evavold, B.; Salaita, K. *Proc. Natl. Acad. Sci. U. S. A.* **2016**, *113* (20), 5610−5615.
(38) Ma, V. P.-Y.; Liu, Y.; Yehl, K.; Galior, K.; Zhang, Y.; Salaita, K. *Angew. Chem., Int. Ed.* **2016**, *55* (18), 5488−5492.
(39) Chowdhury, F.; Doğanay, S.; Leslie, B. J.; Singh, R.; Amar, K.; Talluri, B.; Park, S.; Wang, N.; Ha, T. *Biochem. Biophys. Res. Commun.* **2018**, *500* (3), 557−563.
(40) Zhang, Y.; Qiu, Y.; Blanchard, A. T.; Chang, Y.; Brockman, J. M.; Ma, V. P.-Y.; Lam, W. A.; Salaita, K. *Proc. Natl. Acad. Sci. U. S. A.* **2018**, *115* (2), 325−330.
(41) Wang, Y.; LeVine, D. N.; Gannon, M.; Zhao, Y.; Sarkar, A.; Hoch, B.; Wang, X. *Biosens. Bioelectron.* **2018**, *100*, 192−200.
(42) Su, H.; Liu, Z.; Liu, Y.; Ma, V. P.-Y.; Blanchard, A.; Zhao, J.; Galior, K.; Dyer, R. B.; Salaita, K. *Nano Lett.* **2018**, *18* (4), 2630−2636.
(43) Murad, Y.; Li, I. T. S. *Biophys. J.* **2019**, *116* (7), 1282−1291.
(44) Maier, B.; Potter, L.; So, M.; Seifert, H. S.; Sheetz, M. P. *Proc. Natl. Acad. Sci. U. S. A.* **2002**, *99* (25), 16012.
(45) Salaita, K.; Wang, Y.; Mirkin, C. A. *Nat. Nanotechnol.* **2007**, *2*, 145.
(46) Kufer, S. K.; Puchner, E. M.; Gumpp, H.; Liedl, T.; Gaub, H. E. *Science* **2008**, *319* (5863), 594.
(47) Marko, J. F.; Siggia, E. D. *Macromolecules* **1995**, *28* (26), 8759−8770.
(48) Kratky, O.; Porod, G. *Recl. Trav. Chim. Pays-Bas* **1949**, *68* (12), 1106−1122.
(49) Petrosyan, R. *Rheol. Acta* **2017**, *56* (1), 21−26.
(50) Hu, L.; Vecchiarelli, A. G.; Mizuuchi, K.; Neuman, K. C.; Liu, J. *Proc. Natl. Acad. Sci. U. S. A.* **2015**, *112* (51), No. E7055.
(51) Sugawara, T.; Kaneko, K. *Biophysics (Biophys. Soc. Jpn.)* **2011**, *7*, 77−88.
(52) Wang, W.; Duan, W.; Ahmed, S.; Mallouk, T. E.; Sen, A. *Nano Today* **2013**, *8* (5), 531−554.
(53) Ietswaart, R.; Szardenings, F.; Gerdes, K.; Howard, M. *PLoS Comput. Biol.* **2014**, *10* (12), No. e1004009.
(54) Lim, H. C.; Surovtsev, I. V.; Beltran, B. G.; Huang, F.; Bewersdorf, J.; Jacobs-Wagner, C. *eLife* **2014**, *3*, No. e02758.
(55) Vecchiarelli, A. G.; Seol, Y.; Neuman, K. C.; Mizuuchi, K. *BioArchitecture* **2014**, *4* (4−5), 154−159.
(56) Jindal, L.; Emberly, E. *PLoS Comput. Biol.* **2015**, *11* (12), No. e1004651.
(57) Surovtsev, I. V.; Campos, M.; Jacobs-Wagner, C. *Proc. Natl. Acad. Sci. U. S. A.* **2016**, *113* (46), E7268−e7276.
(58) Le Gall, A.; Cattoni, D. I.; Guilhas, B.; Mathieu-Demazière, C.; Oudjedi, L.; Fiche, J.-B.; Rech, J.; Abrahamsson, S.; Murray, H.; Bouet, J.-Y.; Nollmann, M. *Nat. Commun.* **2016**, *7*, 12107.
(59) Walter, J. C.; Dorignac, J.; Lorman, V.; Rech, J.; Bouet, J. Y.; Nollmann, M.; Palmeri, J.; Parmeggiani, A.; Geniet, F. *Phys. Rev. Lett.* **2017**, *119* (2), No. 028101.
(60) Hu, L.; Vecchiarelli, A. G.; Mizuuchi, K.; Neuman, K. C.; Liu, J. *Biophys. J.* **2017**, *112* (7), 1489−1502.
(61) MacCready, J. S.; Hakim, P.; Young, E. J.; Hu, L.; Liu, J.; Osteryoung, K. W.; Vecchiarelli, A. G.; Ducat, D. C. *eLife* **2018**, *7*, No. e39723.
(62) Castro, C. E.; Su, H.-J.; Marras, A. E.; Zhou, L.; Johnson, J. *Nanoscale* **2015**, *7* (14), 5913−5921.
(63) Marras, A. E.; Zhou, L.; Su, H.-J.; Castro, C. E. *Proc. Natl. Acad. Sci. U. S. A.* **2015**, *112* (3), 713.
(64) Ketterer, P.; Willner, E. M.; Dietz, H. *Science Advances* **2016**, *2* (2), No. e1501209.
(65) Song, J.; Li, Z.; Wang, P.; Meyer, T.; Mao, C.; Ke, Y. *Science* **2017**, *357* (6349), eaan3377.
(66) Cangialosi, A.; Yoon, C.; Liu, J.; Huang, Q.; Guo, J.; Nguyen, T. D.; Gracias, D. H.; Schulman, R. *Science* **2017**, *357* (6356), 1126.
(67) Wan, N.; Hong, Z.; Wang, H.; Fu, X.; Zhang, Z.; Li, C.; Xia, H.; Fang, Y.; Li, M.; Zhan, Y.; Yang, X. *Small* **2017**, *13* (41), 1700866.
(68) Kovacic, S.; Samii, L.; Curmi, P. M. G.; Linke, H.; Zuckermann, M. J.; Forde, N. R. *IEEE Trans. NanoBiosci.* **2015**, *14* (3), 305−312.

DOI: 10.1021/acs.nanolett.9b02311
Nano Lett. 2019, 19, 6977−6986

(69) Goel, A.; Vogel, V. *Nat. Nanotechnol.* **2008**, *3*, 465.
(70) Hess, H.; Saper, G. *Acc. Chem. Res.* **2018**, *51* (12), 3015−3022.
(71) Blanchard, A. T.; Salaita, K. *Science*, in press, DOI: 10.1126/science.aax3343.

DOI: 10.1021/acs.nanolett.9b02311
Nano Lett. 2019, 19, 6977−6986